Electronic Supplementary Material (ESI) for Journal of Materials Chemistry A.

Supporting Information

Defective NiMn LDH Prepared Using the Hydrogen Evolution Coupled Electrodeposition for Highly Efficient Oxygen Evolution Reaction

*Mao Sun, Jike Wang**

Experimental section

Electrocatalysts preparation

Preparation of defective NiMn LDH: The hydrogen evolution coupled electrodeposition (HECED) method was used to synthesize defective NiMn LDH on the cleaned carbon cloth (CC) substrate. A CC (0.5×1.5 cm^{-2}) was used as the working electrode, another the CC (1.0×1.5 cm^{-2}) as the counter electrode, and Ag/AgCl (3 M KCl) as the reference electrode. To prepare the electrolyte solution, 10 mmol of $MnCl_2 \cdot 4H_2O$ and 1.2 mmol of $NiCl_2 \cdot 6H_2O$ were dissolved in 50 mL of ultrapure water and stirred for 30 min to ensure homogeneity. The electrodeposition was carried out at a constant voltage of –1.1 V (vs. Ag/AgCl) for 200 s at 80 °C. The cathodic bias reduced water to hydrogen, increasing the local pH on the working electrode and leading to the precipitation of defective NiMn LDH on the CC substrate. The resulting defective NiMn LDH was then washed and dried at 60°C for 2 hours.

Preparation of D-NiMn LDH/FeS: The D-NiMn LDH/FeS heterostructure was synthesized using the successive ionic layer adsorption and reaction (SILAR) method. To prepare the Na_2S solution, 0.27 g of Na_2S was dissolved in 50 mL of pure water to obtain a 20 mM solution. Similarly, a 20 mM ethanolic solution of iron acetylacetonate was prepared. Subsequently, the D-NiMn LDH samples were immersed in fresh cationic and anionic solutions for 10 s each, respectively. After each immersion, the corresponding solvent was used to rinse for 10 s. These four immersion steps are considered as one deposition. Such 6 cycles were repeated to get the final D-NiMn LDH/FeS electrode. For comparison, the D-NiMn LDH/FeOOH was prepared using a similar procedure as the D-NiMn LDH/FeS, with the exception that the Na_2S solution was replaced with 1 M KOH.

Characterization

The X-ray diffraction analysis (XRD, Rigaku Smartlab SE, Japan) using Cu Kα radiation at 40 kV and 30 mA allowed for identification of the crystalline structure. The elemental

composition was determined through the utilization of X-ray photoelectron spectroscopy (XPS, ESCALAB 250xi, Thermo Fisher Scientific). Additionally, scanning electron microscopy (SEM) and transmission electron microscopy (TEM) were performed using FESEM (Hitachi SU8220) and TITAN G2 microscope (FEI, USA) systems. Electron paramagnetic resonance (EPR) measurements were taken at low temperature (77 K) using a Bruker EMXplus spectrometer. The elemental contents in the electrolyte were analyzed through inductively coupled plasma optical emission spectroscopy (ICP-OES, Jena Analytical Instruments Co., LTD, Germany). X-ray absorption fine structure (XAFS) measurements at Ni-edge, Mn K-edge, and Fe K-edge were conducted at the XAFCA beamline in the Singapore Synchrotron Light Source. The software package Demeter was utilized to analyze the XAFS data in accordance with standard data analysis procedures. Athena was used to normalize the spectra, after which shell fittings were performed with Artemis. The $\chi(k)$ function was Fourier transformed (FT) using k2 weighting, and all fittings were performed in R-space. Wavelet transform (WT) analysis using the Matlab code developed by Munoz et al was employed to further investigate the first-shell backscattering atoms and detect light and heavy scatters (*Am. Mineral.*, 2003, **88**, 694-700.).

Electrochemical measurements

The electrochemical properties of all tested samples were carried out at an electrochemical analyzer (CHI760D, CH Instruments, Inc.). The experiments were conducted employing a standard three-electrode system. The prepared catalyst was used as the working electrode, while a graphite rod and a Hg/HgO electrode were used as the counter electrode and reference electrode, respectively. The polarization curves of the HER/OER properties of the samples were obtained using linear scanning voltammetry (LSV) or cyclic voltammetry (CV) at a scan rate of 5 mV s^{-1} in 1 M KOH solution with iR compensation. The stability tests were performed by chronopotentiometric measurement at 20 mA cm^{-2} in 1 M KOH. The electrochemical active surface area (ECSA) was estimated from the double-layer capacitance (C_{dl}) values, where the

C_{dl} values can be calculated by testing the relationship between current density and sweep rate (20-100 mV s^{-1}). The electrical impedance spectra (EIS) were tested at different applied potentials at fixed frequencies ranging from 0.1 Hz to 100 kHz and at an AC voltage of 5 mV. All potentials after the tests were calibrated to the reversible hydrogen electrode using the equation: $E_{RHE} = E_{Hg/HgO} + 0.0591 \times pH + 0.098$.

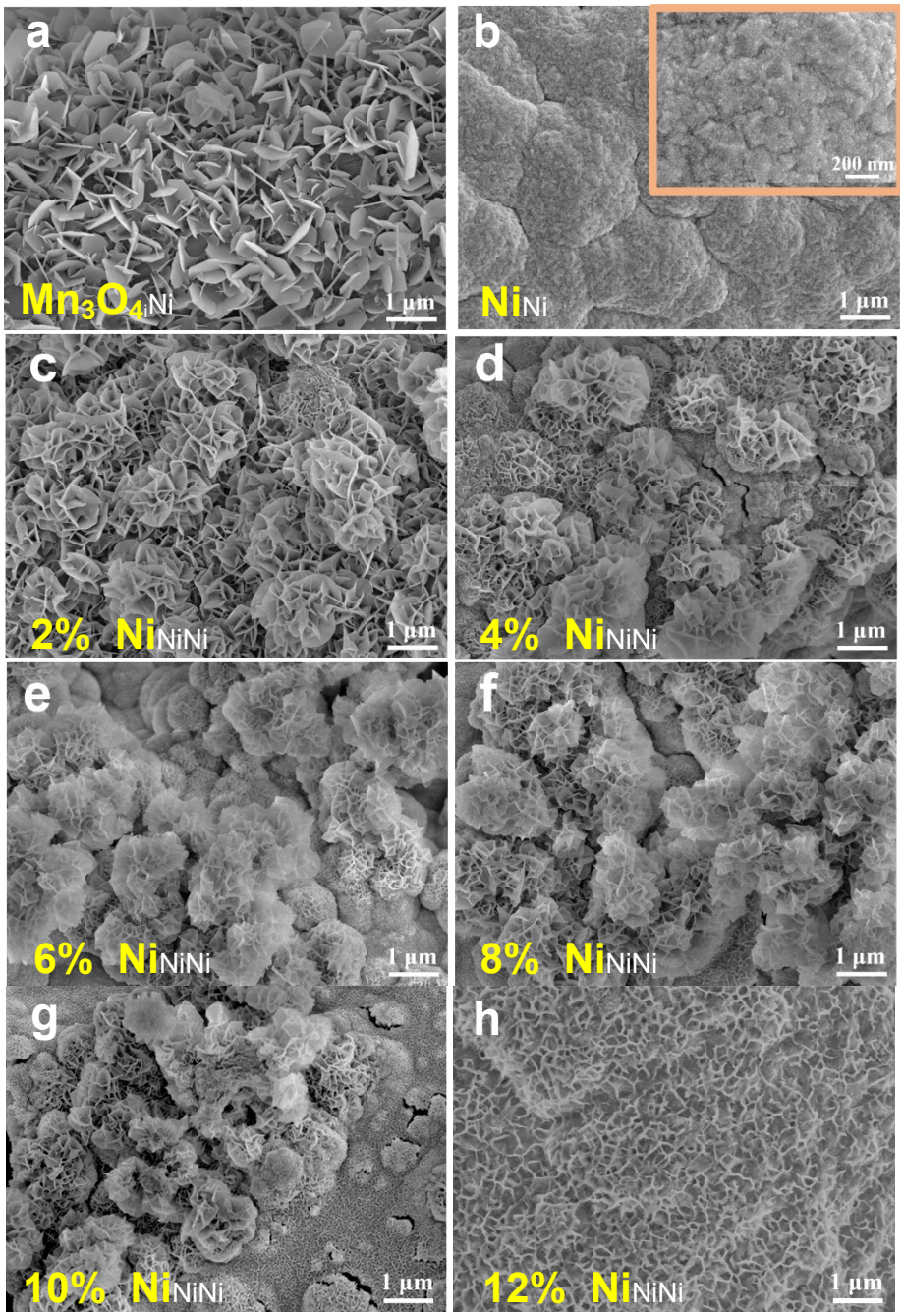

Figure S1. SEM images of (a) Mn_3O_4, (b) Ni, and (c-h) NiMn hydroxides with various Ni amounts.

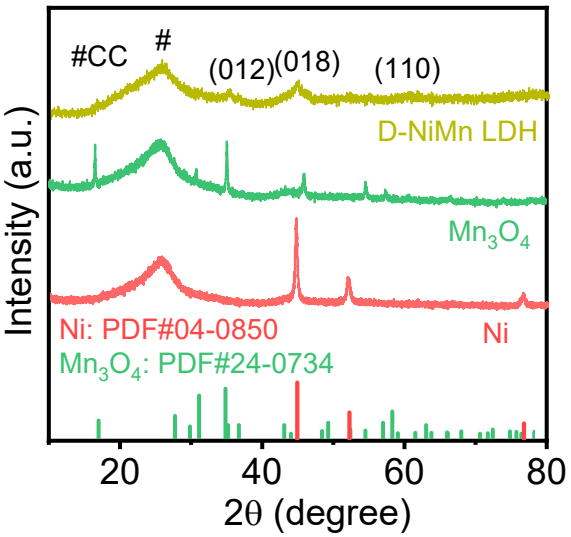

Figure S2. XRD patterns of Ni, Mn_3O_4, and D-NiMn LDH.

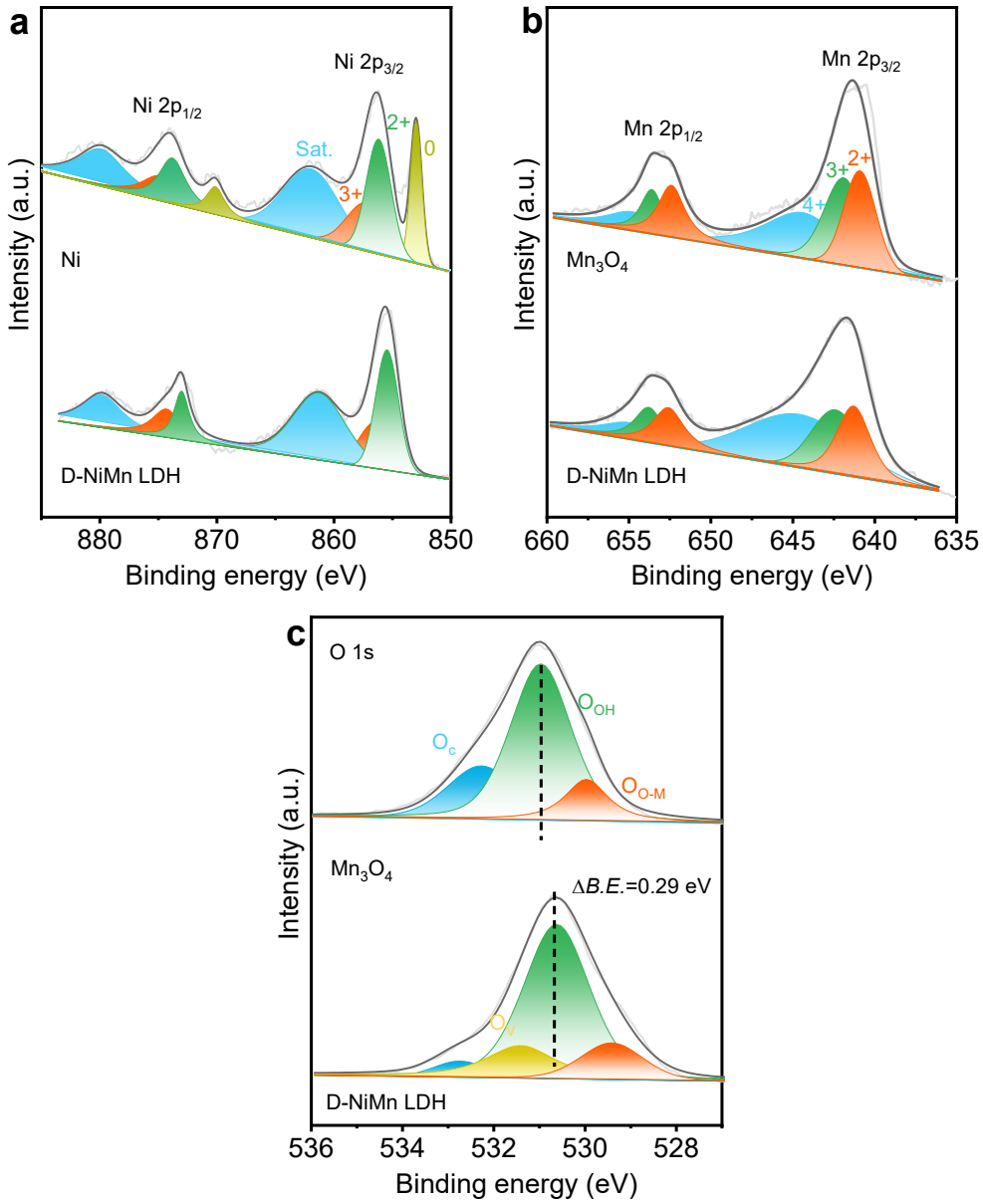

Figure S3. (a-c) XPS spectra of Ni 2p (a) of Ni and D-NiMn LDH, Mn 2p (b) and O 1s (c) of Mn_3O_4 and D-NiMn LDH.

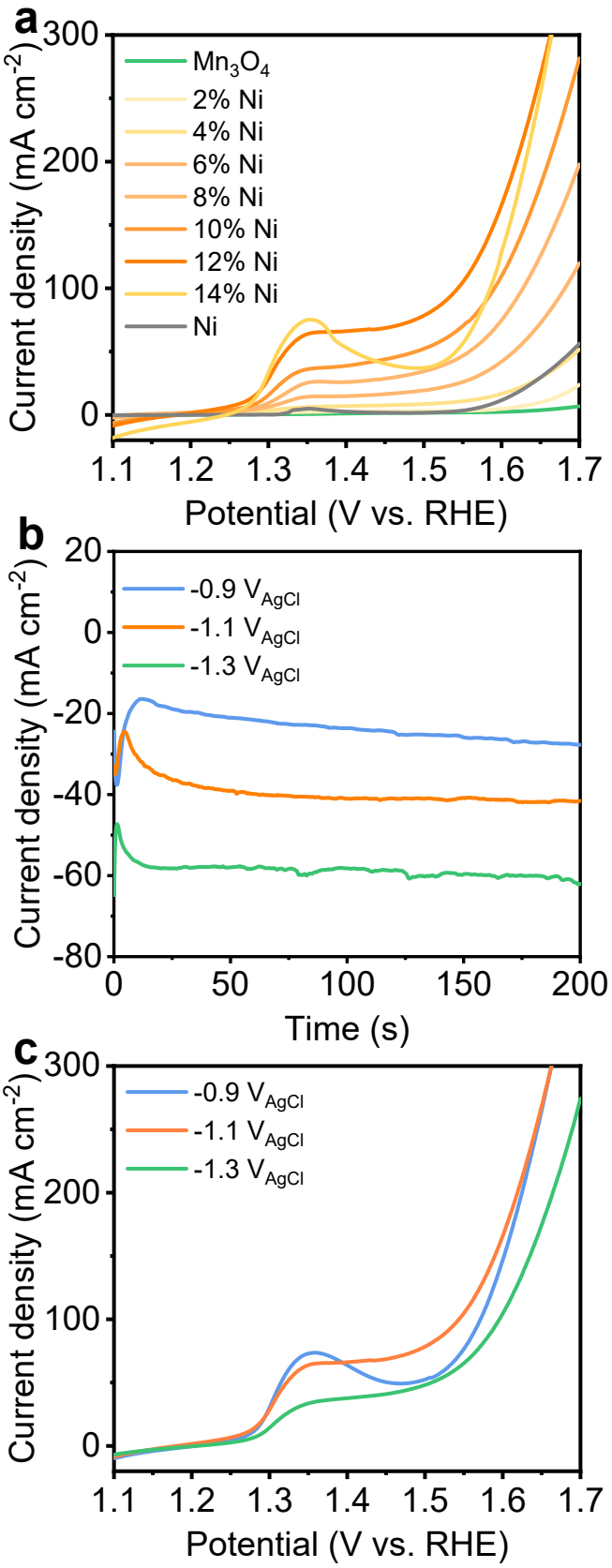

Figure S4. (a) LSV curves for OER of Ni, Mn_3O_4 and NiMn hydroxides with different Ni content; (b) *J-t* curves of D-NiMn LDH under different deposition potential; (c) polarization curves of the corresponding electrode.

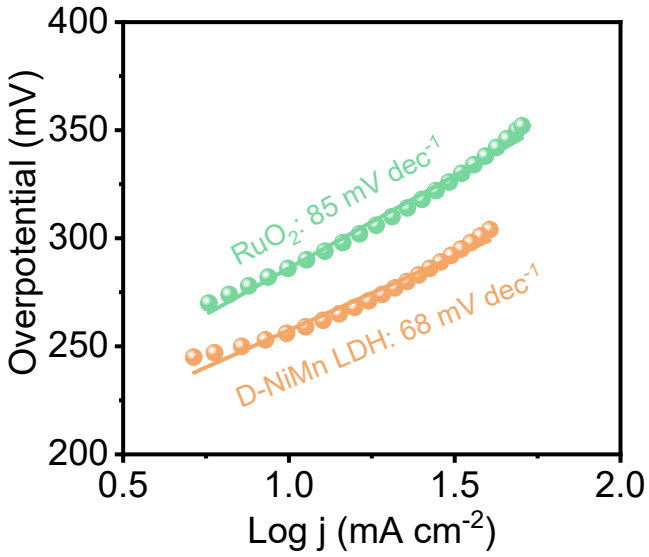

Figure S5. Tafel plots for D-NiMn LDH and RuO_2 in 1 M KOH;

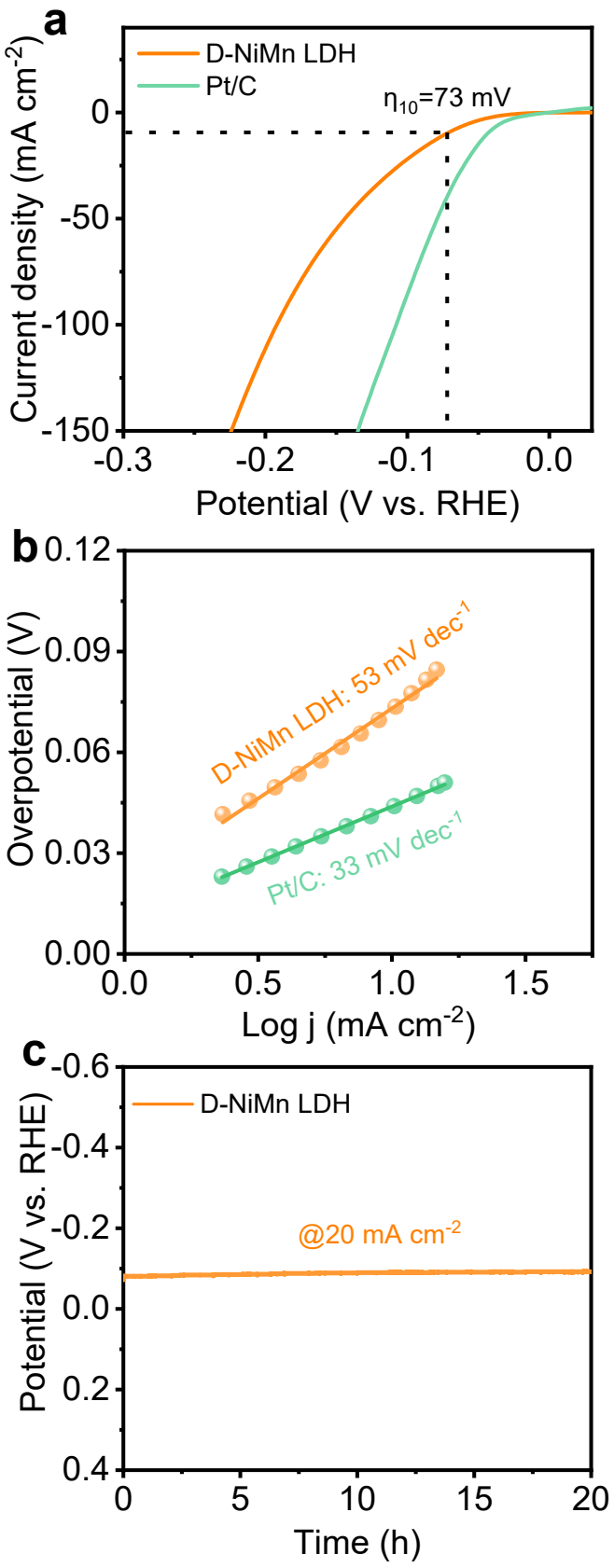

Figure S6. (a) Polarization curves and (b) Tafel slopes of D-NiMn LDH and Pt/C; (c) chronoamperometric curve of D-NiMn LDH at the overpotential required to maintain 20 mA cm^{-2} for 20 h.

Table S1. Comparison of the HER/OER performances of the D-NiMn LDH with recently reported NiMn-based electrocatalysts in 1 M KOH.

Catalyst	η_{10} (mV)	Tafel slope (mV dec^{-1})	References
D-NiMn LDH	256	68	This work.
Ni_3S_2/MnS-O	228	53	Appl. Catal. B 2019, 257, 117899.
NiMn LDH	240	31	ACS Nano 2021, 15, 14996−15006.
Carbon Sheets@$NiMnO_3$	250	40	ACS Appl. Mater. Inter. 2016, 8, 11396-1140.
$NiMnO_3$	256	141	Ceramics International 2020, 46, 28006.
Ni-NiO-Ov	265	61.3	Appl. Surf. Sci 2022, 577, 151952.
MnNiSe	276	-	J. Mater. Chem. A, 2020, 8, 25298–25305.
NiMn-MOFs+MCCF	280	86	Angew. Chem. Int. Ed. 2020, 59, 18234-18239.
$Ni_{0.75}Mn_{0.25}$ Oxide	297	91	ACS Energy Lett. 2018, 3, 2150-2158.
Ni-Mn-LDH/g-C_3N_4	316	65	Appl. Catal. B 2019, 242, 485-498.
NiMn-LDHs	330	126	J. Alloys Compd 2021, 852, 156949.
Ni doped MnO_2	330	47.6	ChemCatChem 2019, 11, 1689-1700.
Mn-doped Ni_2P	330	116.7	Catalysis Today 2020, 355, 815.
$NiMnO_3$/$NiMn_2O_4$	380	73.3	ACS Appl. Mater. Inter. 2016, 8, 26740-26757.
$NiMnO_x$	383	71	Nanoscale 2020, 12, 2472-2478.
NiMn LDH	385	59	Applied Clay Science 2018, 165, 277.
NiMn LDH	401	126	J. Mater. Chem. A, 2019, 7, 26975-26983.
D-NiMn LDH	73	53	This work.
Ni-Mn-LDH/g-C_3N_4	65	63	Appl. Catal. B. 2019, 242, 485-498.
Mn-doped NiS_2	71	57	J. Mater. Chem. A 2019, 7, 25628-25640.
Mn-Ni/C	80	68	ACS Nano 2018, 12, 11625-11631.
Ni-Mn_3O_4	91	110	Chem. Commun. 2016, 52, 10566-10569.
Mn-NiS	99	64.8	Electrochem. Soc. 2022, 169, 106512.
Mn-Ni_2P	103	135	Chem. Commun. 2017, 53, 11048-11051.
Ni_3S_2/MnS-O	116	41	Appl. Catal. B 2019, 257, 117899.
Mn-Ni_3S_2	152	80	Chem. Commun., 2018, 54, 10100-10103.
Mn-doped Ni_2P	205	-	Catalysis Today 2020, 355, 815.
NiMn LDH	220	128	J. Mater. Chem. A, 2019, 7, 26975–26983.

The catalysts' OER and HER performances are compared in the yellow and green grounds, respectively.

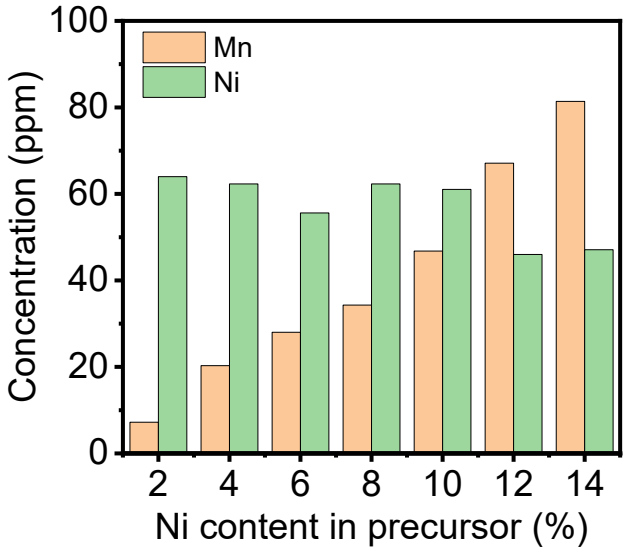

Figure S7. ICP analysis of the samples.

Figure S7 presents the ICP analysis results of the samples, which were synthesized using precursor solutions with varying ratios of Ni and Mn ions. It is noteworthy that the proportion of Ni : Mn in the actual samples consistently surpasses the corresponding feeding ratio present in the precursor solution. At the precursor ion ratio (Ni:Mn = 12:88) associated with the optimal OER performance, the actual ratio in the D-NiMn LDH was found to be Ni:Mn = 67:46. This observation suggests that Ni ions display a heightened sensitivity to the deposition potential and demonstrate higher migration rate compared to Mn ions under the same potential conditions.

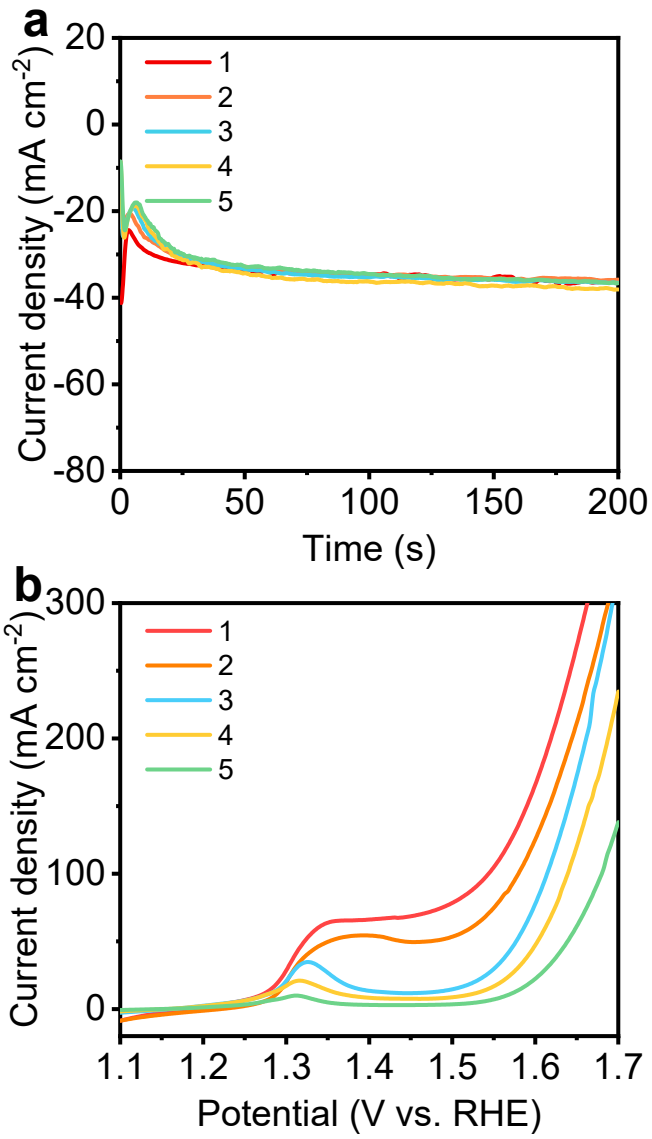

Figure S8. (a) *J-t* curves of 5 consecutive depositions in the precursor solution containing $NiCl_2$ and $MnCl_2$; (b) LSV curves of the corresponding electrode.

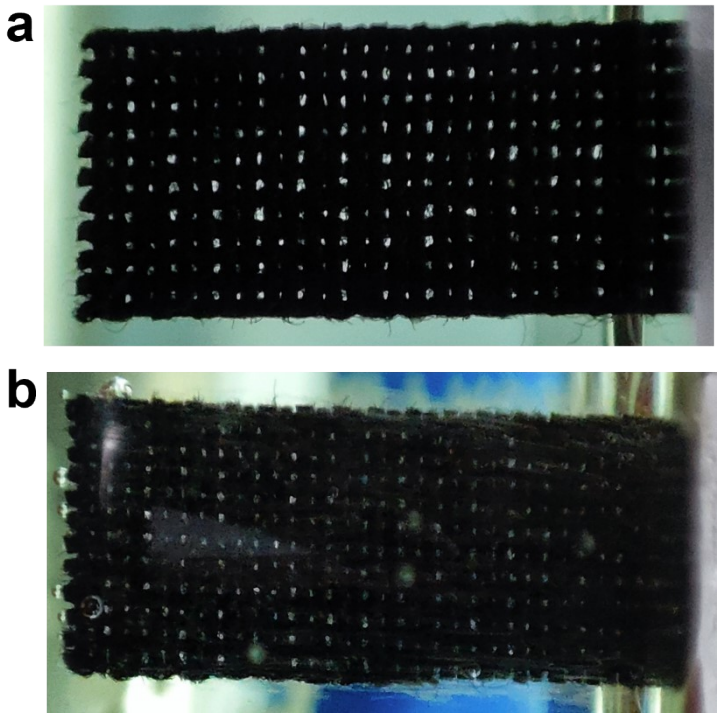

Figure S9. The optical photograph of NiMn LDH obtained in nitrate (a) and chloride salts (b).

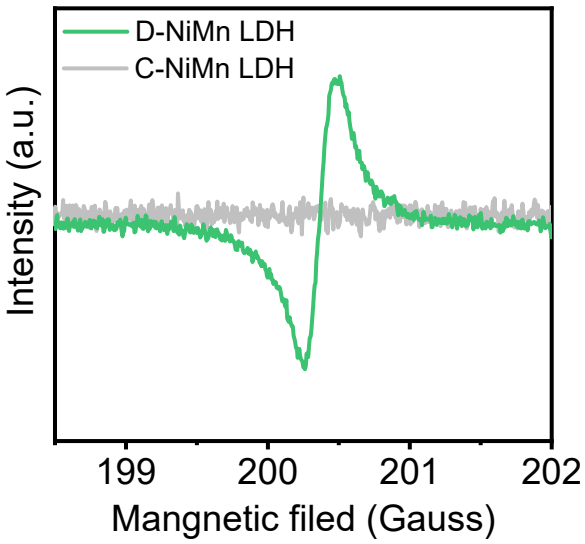

Figure S10. EPR spectra of D-NiMn LDH and C-NiMn LDH.

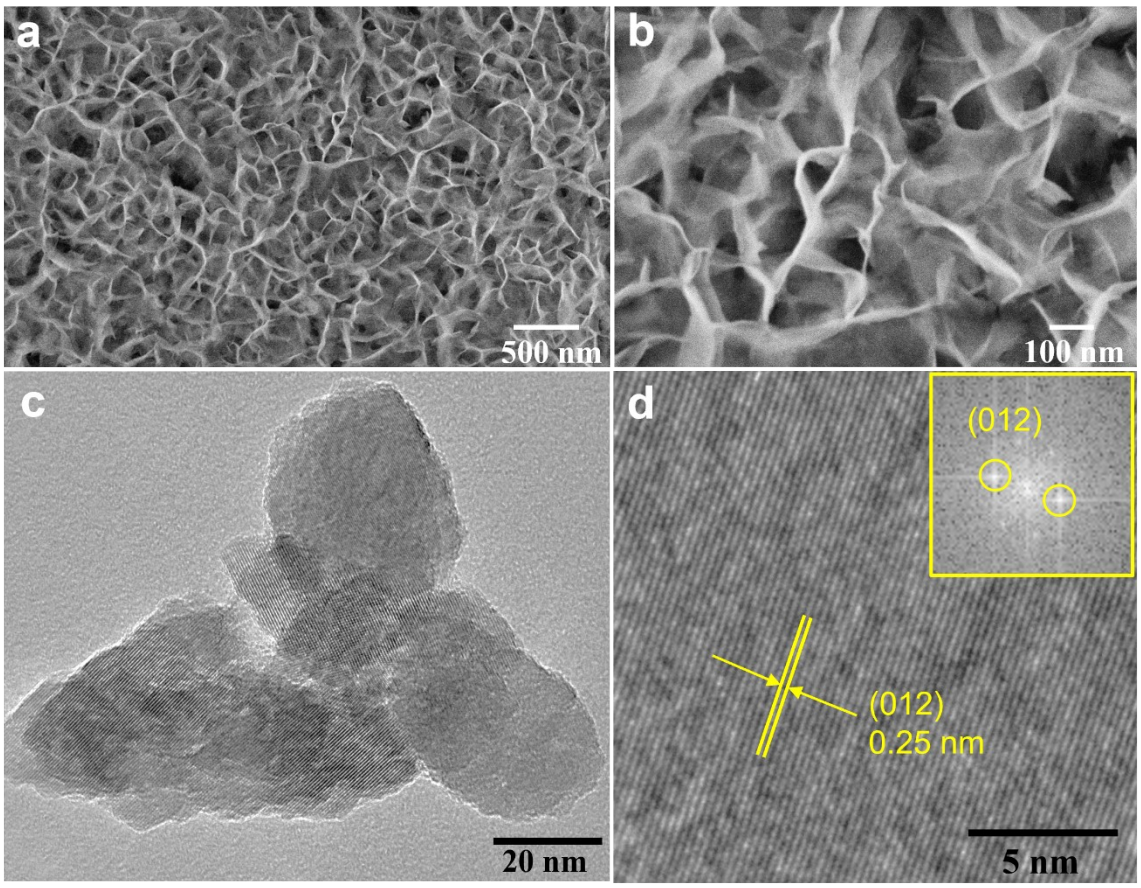

Figure S11. (a,b) SEM images, (c,d) TEM images of C-NiMn LDH; Inset of d show FFT pattern of the corresponding part.

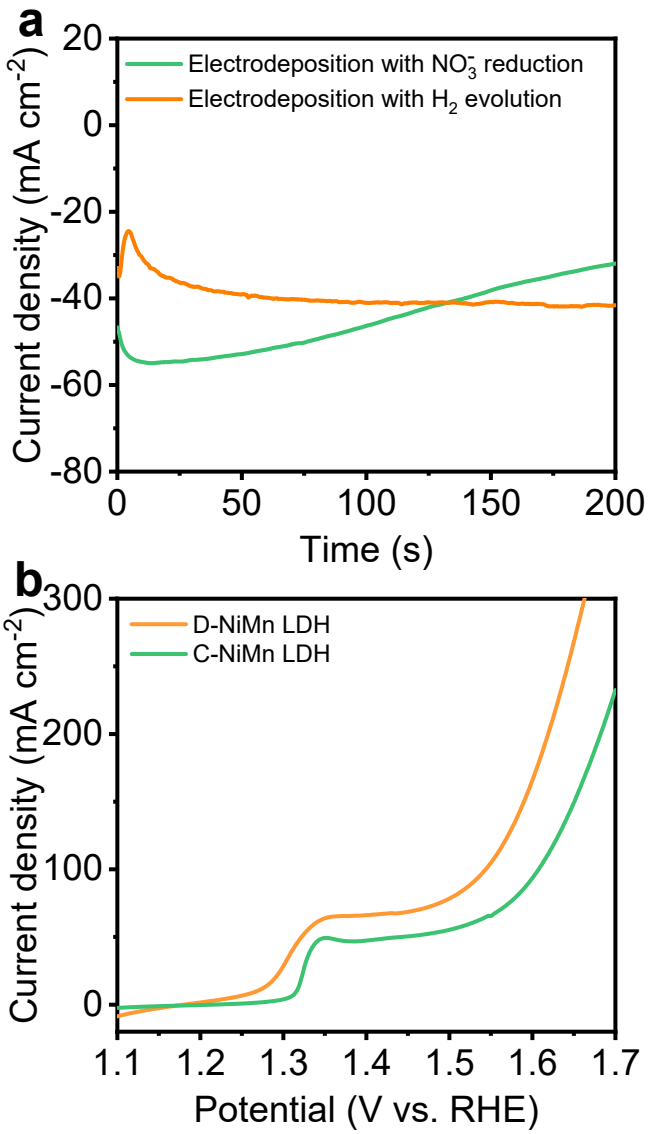

Figure S12. (a) *J-t* curves of NiMn LDH deposited in nitrate and chloride salts; (b) LSV curves of the corresponding electrode.

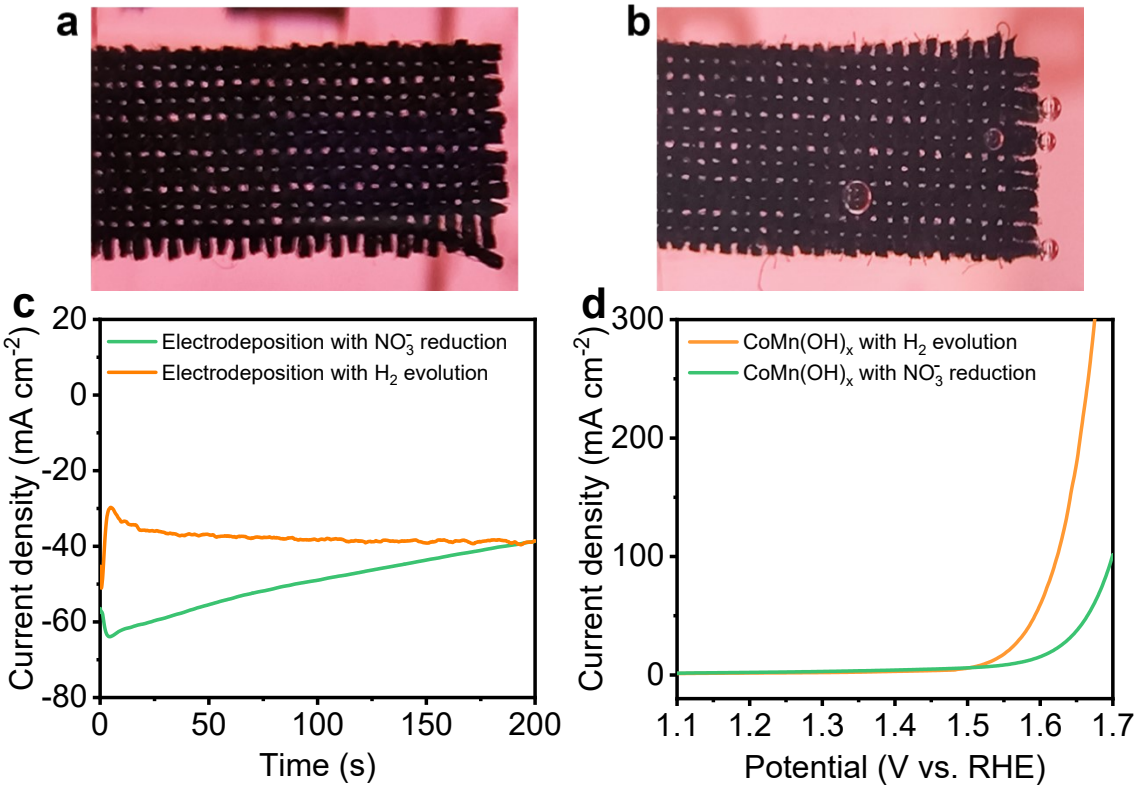

Figure S13. The optical photograph of CoMn hydroxides obtained in nitrate (a) and chloride salts (b); (c) *J-t* curves of $CoMn(OH)_x$ deposited in nitrate and chloride salts; (d) LSV curves of the corresponding electrode.

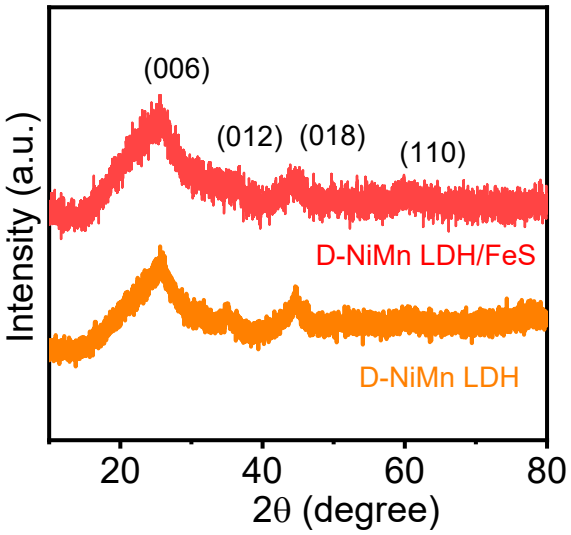

Figure S14. XRD patterns of D-NiMn LDH and D-NiMn LDH/FeS.

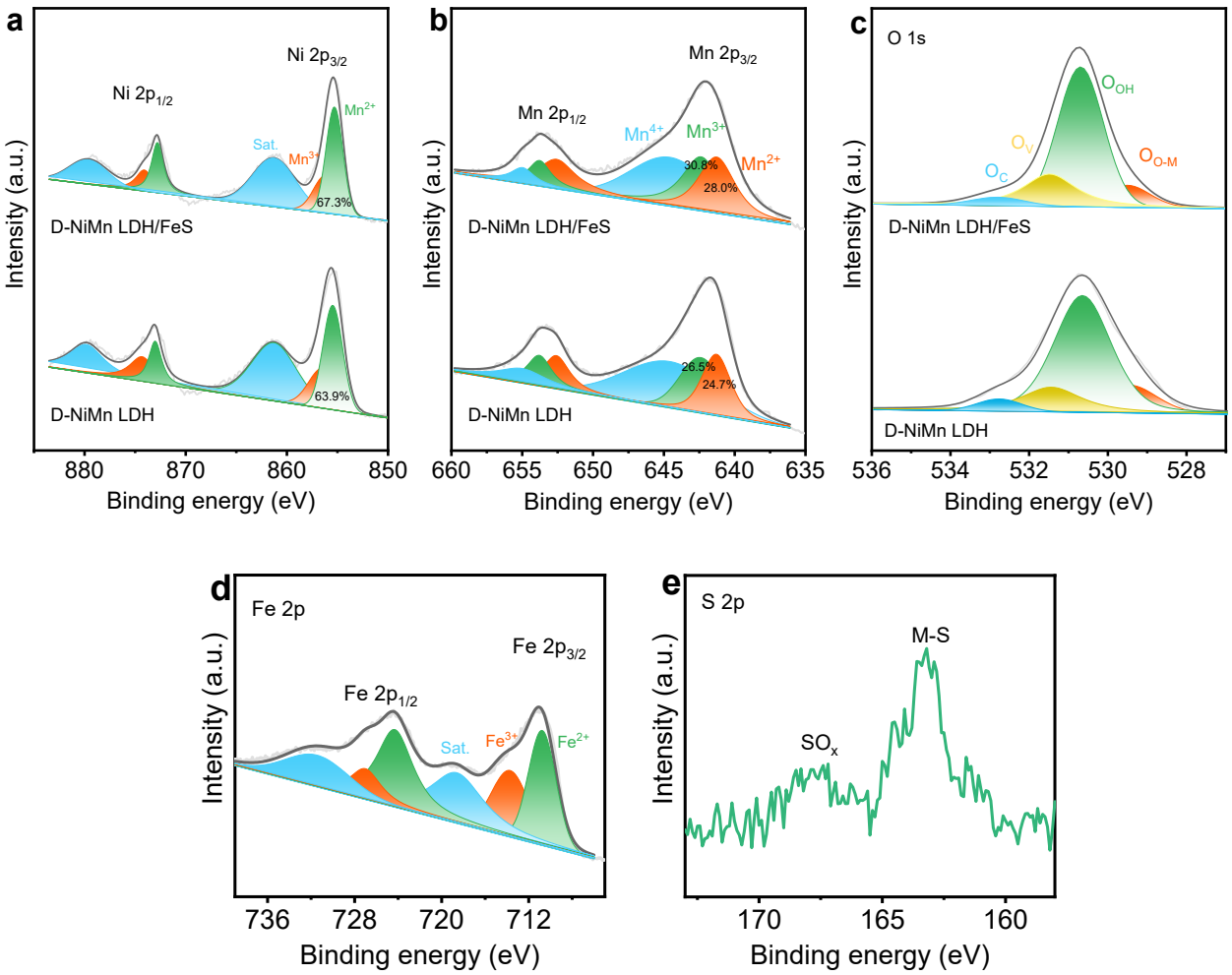

Figure S15. (a-c) XPS spectra of Ni 2p (a), Mn 2p (b), and O 1s (c) of D-NiMn LDH and D-NiMn LDH/FeS; (d,e) XPS spectra of Fe 2p and S 2s of D-NiMn LDH/FeS.

To elucidate the valence change after forming D-NiMn LDH/FeS, a comparison was made between the XPS spectra of D-NiMn LDH and D-NiMn LDH/FeS. As illustrated in **Figure S15,** it is evident that the relative concentrations of Ni^{2+} and Mn^{2+} in NiMn LDH exhibit an enhanced trend after the introduction of FeS. This observation can be attributed primarily to the strong reducing properties of S^{2-}, which effectively facilitates the conversion of cations from a high valence state to lower valence states. Additionally, a clear observation reveals that the valence state of Fe in FeS predominantly appears as Fe^{2+}. In the S 2p region, the peak at 163.2 eV from S^{2-} corroborates the existence of the metal-sulfur bonds. These results provide further confirmation of the successful formation of FeS.

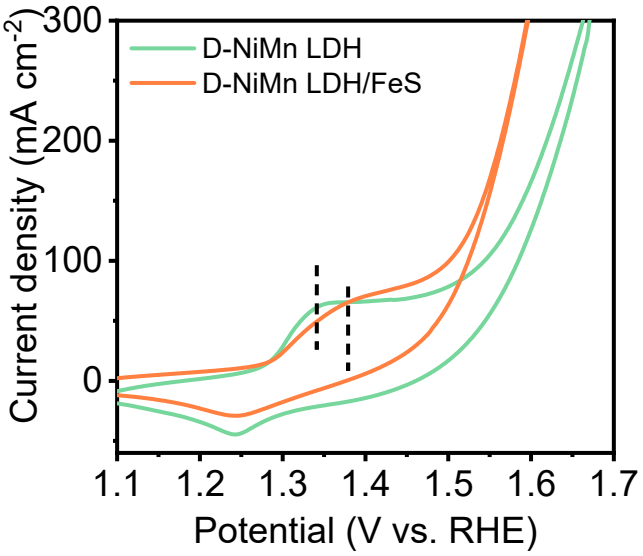

Figure S16. (a) Cyclic voltammetry curves of D-NiMn LDH and D-NiMn LDH/FeS.

Table S2. Comparison of the OER performances of the D-NiMn LDH/FeS with other recently reported electrocatalysts in 1 M KOH.

Catalyst	η_{10} (mV)	Tafel slope (mV dec^{-1})	Reference
D-NiMn LDH/FeS	184	49	This work.
$NiCo_{2-x}Fe_xO_4$	274	42	Angew. Chem. Int. Ed. 2021, 60, 11841-11846.
FeNi-LDH	203	24.9	Angew. Chem. Int. Ed. 2023,e202215728.
NiCoFe-HO@NiCo-LDH	276	49.7	Angew. Chem. Int. Ed. 2022, 61, e202213049
$FeS_2@NiS_2$	237	31.4	Small 2023, 2207472.
Fe-(Ni-MOFs)/FeOOH	210	50	Angew. Chem. Int. Ed. 2022, 61, e202116934.
$(CrFeCoNi)_{97}O_3$	196	29	Adv. Mater. 2021, 33, 2101845.
$Co_{0.85}Se_{1-x}@C$	231	57	Adv. Mater. 2021, 33, 2007523.
NiOOH/(LDH/α-FeOOH)	195	30.1	Adv. Mater. 2023, 35, 2209338.
$Mo\text{-}NiFeO_xH_y$	193	32.3	Adv. Mater. 2022, 34, 2202523.
$W\text{-}NiS_{0.5}Se_{0.5}$	171	41	Adv. Mater. 2022, 34, 2107053.
$Ni(Fe)OOH–FeS_x$	220	55	Nat. Commun. 2020, 11, 5075.
$Co(OH)_2/NiP_x$	236	52	Adv. Funct. Mater. 2022, 32, 2206407.
S-NiFe LDH	219	24.8	Adv. Energy Mater.2022, 12, 2202522.
W dopant in NiFe-LDHs	211	36.4	Chem. Eng. J 2023, 452, 139104.
NiMnOP	189	29.2	Nano Energy 2020, 69, 104432.
$CoMnP/Ni_2P/NiFe$	204	60	J. Mater. Chem. A, 2019, 7, 12325–12332.
$Co_4Mn_1Fe_3$ LTH	200	55	J. Mater. Chem. A, 2019, 7, 13130–13141.
$CoMnP/Ni_2P$	209	49	J. Mater. Chem. A, 2021, 9, 22129–22139.
$NiCo_2S_4/ZnS$	140	47	Angew. Chem. Int. Ed. 2021, 60, 19435 – 19441.
$Fe_{60}(CoNi)_{30}Cr_{10}$	187	44	Small 2022, 18, 2105611.
$Ni_{0.91}Fe_{0.09}(OH)_2$	185	58.7	Adv. Mater. 2022, 34, 2200088.
$AD\text{-}LiCoO_2$	184	35.4	Adv. Funct. Mater. 2022, 32, 2200663.
Au/NiFe LDH	189	35	Adv. Mater. 2022, 34, 2110552.
FeAsS/α-FeOOH	200	43.2	Chem. Eng. J 2022, 431, 134304.
$Ni_{0.75}V_{0.25}LDH$	200	48.3	ACS Catal. 2022, 12, 3821−3831.
$Co@CoO/RuO_2$	198	57	Adv. Funct. Mater. 2023, 2214124.
CoFe@NiFe-200	190	45.7	Appl. Catal. B. 2019, 253, 131.
$NiFe(OH)_x/(Ni, Fe)Se_2$	180	42	Small 2021, 17, 2007334.
Gd-NiFe-LDH	210	40.9	J. Mater. Chem. A, 2021, 9, 2999.
NiFe LDH@NiCoP	220	48.6	Adv. Funct. Mater. 2018, 28, 1706847.

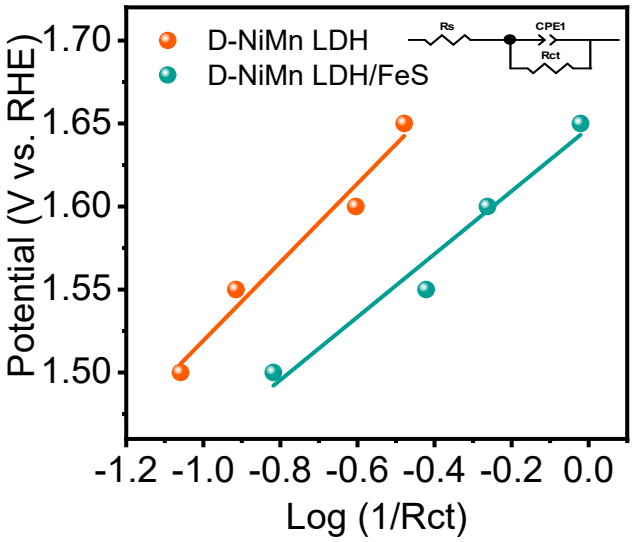

Figure S17. log (1/Rct) vs applied potential for OER regions.

Table S3. EIS measurements values.

Sample		1.50 V_{RHE}	1.55 V_{RHE}	1.6 V_{RHE}	1.65 V_{RHE}
D-NiMn LDH	Rs/ohm	4.61	4.58	4.53	4.63
	Rct/ohm	11.45	8.23	4.02	3.01
D-NiMn LDH/FeS	Rs/ohm	4.67	4.58	4.61	4.69
	Rct/ohm	6.55	2.64	1.83	1.05

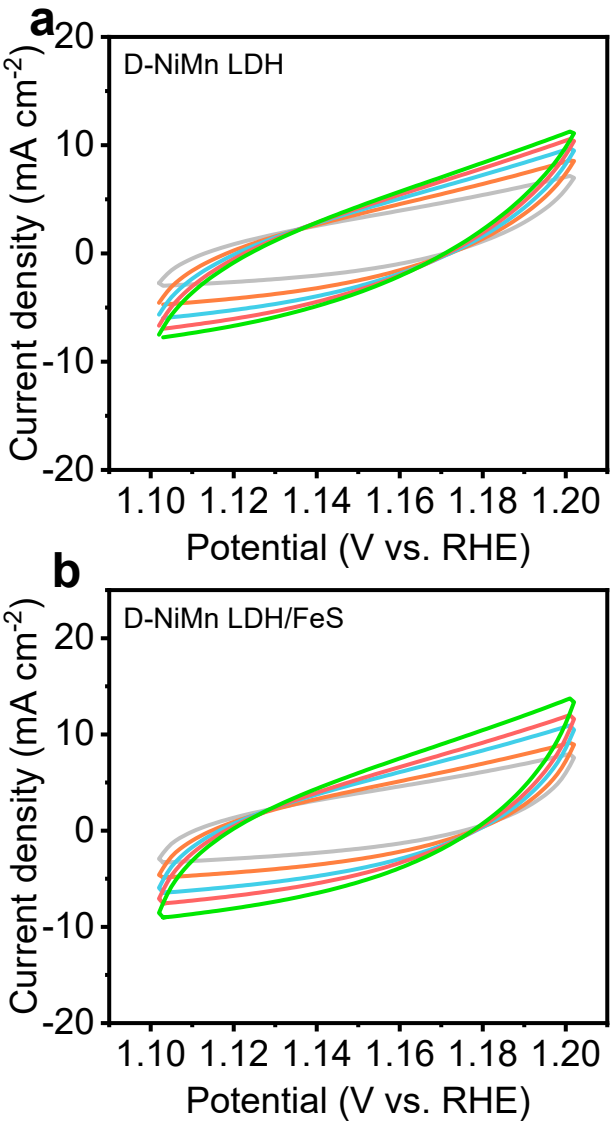

Figure S18. Cyclic voltammograms of D-NiMn LDH (a) and D-NiMn LDH/FeS (b) in the non-faradaic capacitance current at scan rates of 20, 40, 60, 80 and 100 mVs^{-1}.

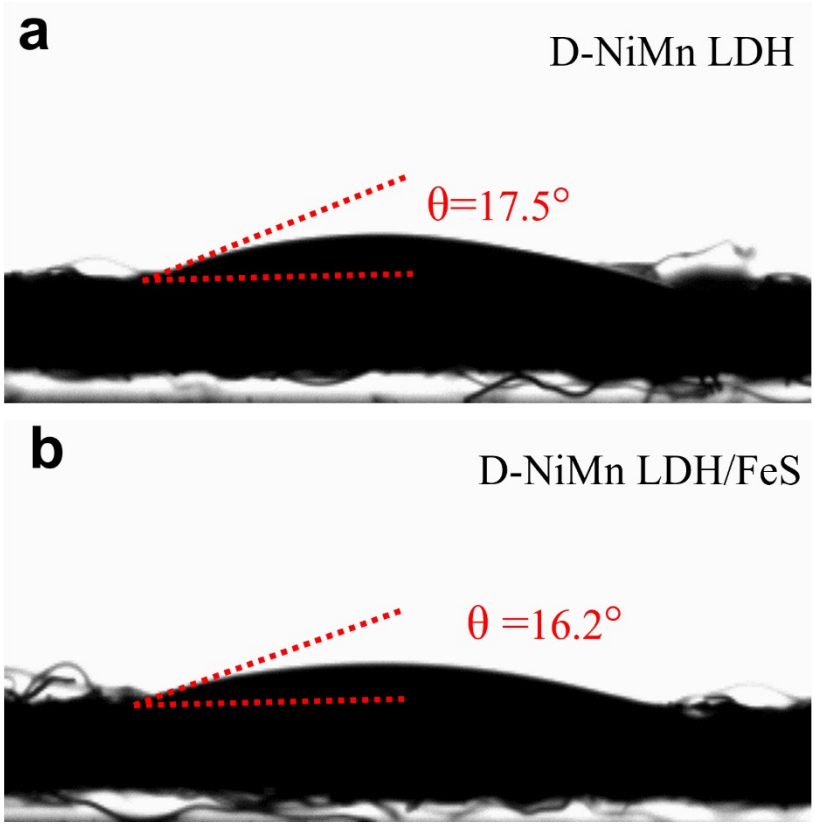

Figure S19. Water contact angle images of (a) D-NiMn LDH and (b) D-NiMn LDH/FeS.

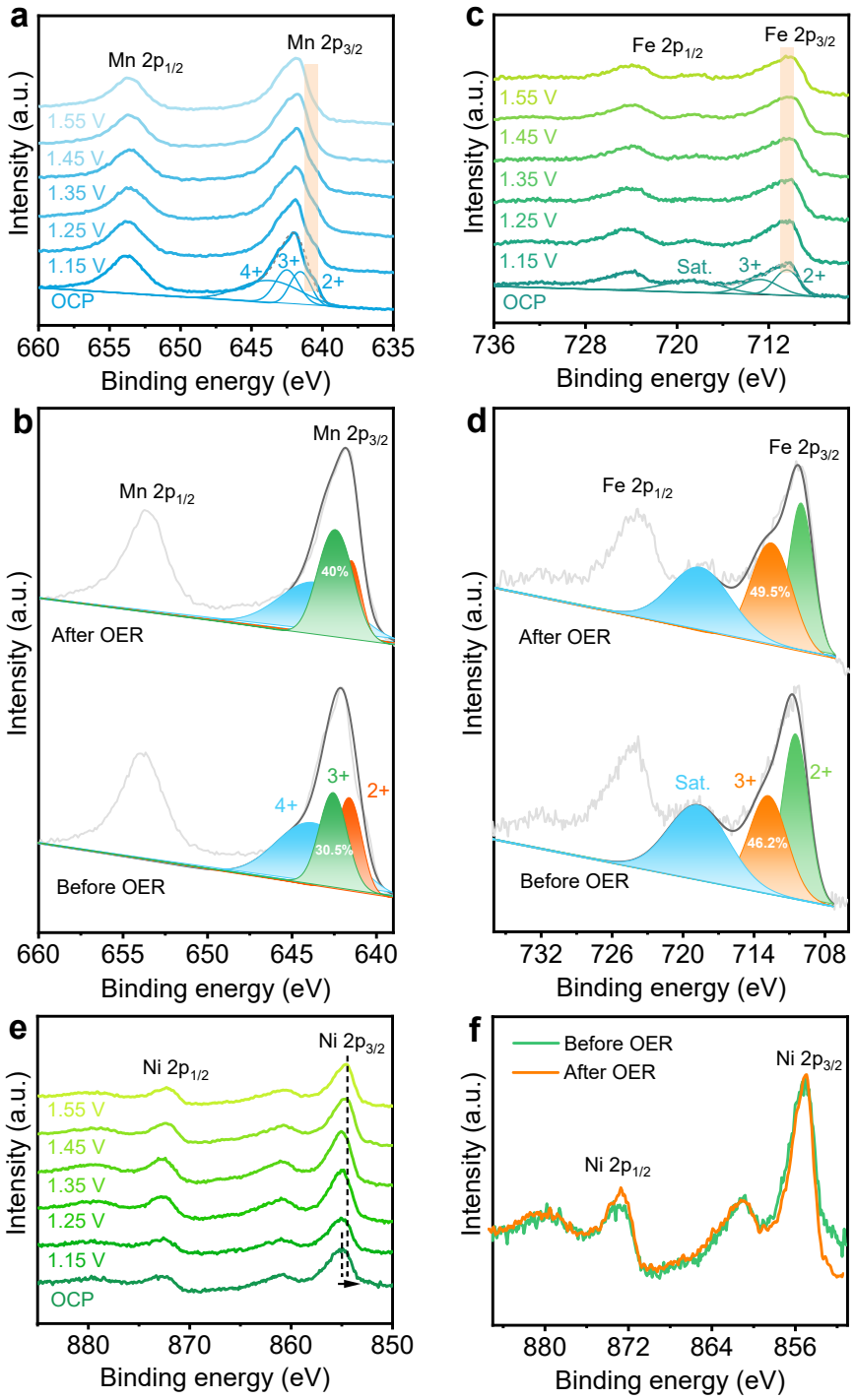

Figure S20. (a,c) Ex-situ XPS spectra of Mn (a) and Fe (c); (b,d) the corresponding XPS spectra at OCP and 1.55 V in Figure a,c. (e) ex-situ XPS spectra of Ni; (f) the corresponding to the XPS spectra at OCP and 1.55 V in Figure e.

To better compare the XPS spectra of Ni before and after OER, the Ni spectra after OER were panned, revealing that the XPS spectra of Ni before and after OER exhibit basically overlap.

Table S4. EXAFS fitting parameters at the Mn K-edge for D-NiMn LDH/FeS before and after OER.

Sample	ΔE_0/eV	Scatter path	N	R/Å	σ^2/Å
Before OER	3.8	Mn-O	0.69±0.24	2.27	0.005
		Mn-O1	1.5±0.18	2.00	0.006
		Mn-O2	1.14±0.14	1.90	0.001
		Mn-Mn	1.97±0.38	3.26	0.002
		Mn-Mn1	3.97±0.50	3.09	0.003
		Mn-Mn2	2.26±0.42	2.90	0.006
After OER	-2.7	Mn-O	0.7	2.28	0.006
		Mn-O1	3.43±0.30	1.91	0.003
		Mn-O2	0.46±0.30	1.78	0.006
		Mn-Mn	1.24±0.27	2.83	0.001
		Mn-Mn1	3.19±0.64	2.96	0.006
		Mn-Mn2	0.58±0.76	3.23	0.005

ΔE_0: the inner potential correction; N: coordination numbers; R: bond distance; σ^2: Debye-Waller factors; The S_0^2 was fixed to 1.0 for the samples. The fitting range is $2 < k < 11.5$ Å^{-1}, $1 < R < 3$ Å.

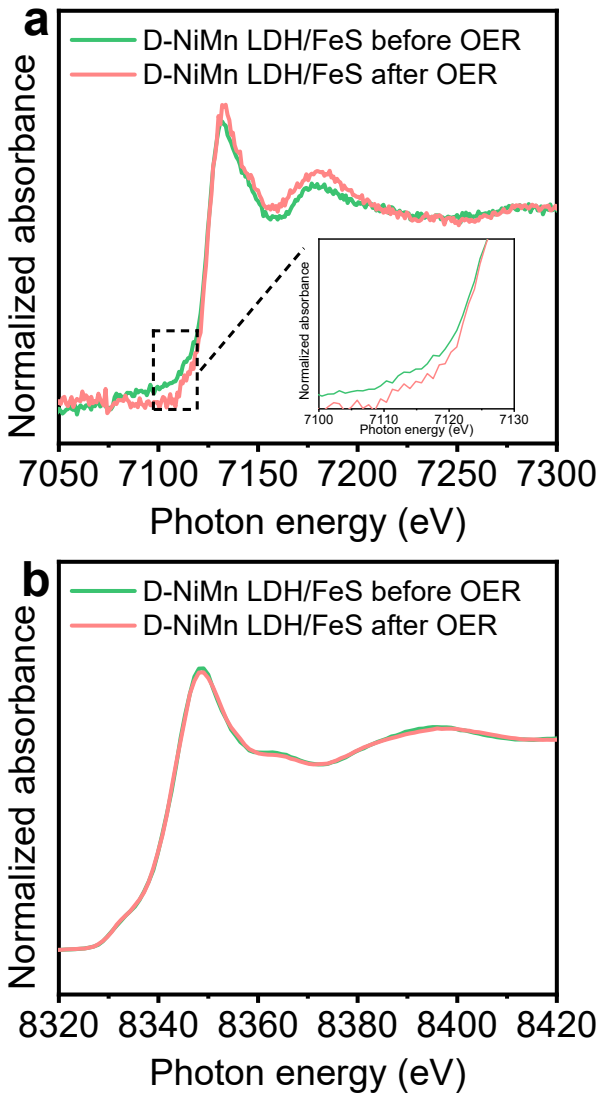

Figure S21. Normalized X-ray absorption near-edge structure (XANES) at the (a) Fe K-edge and (b) Ni K-edge of D-NiMn LDH/FeS before and after OER.

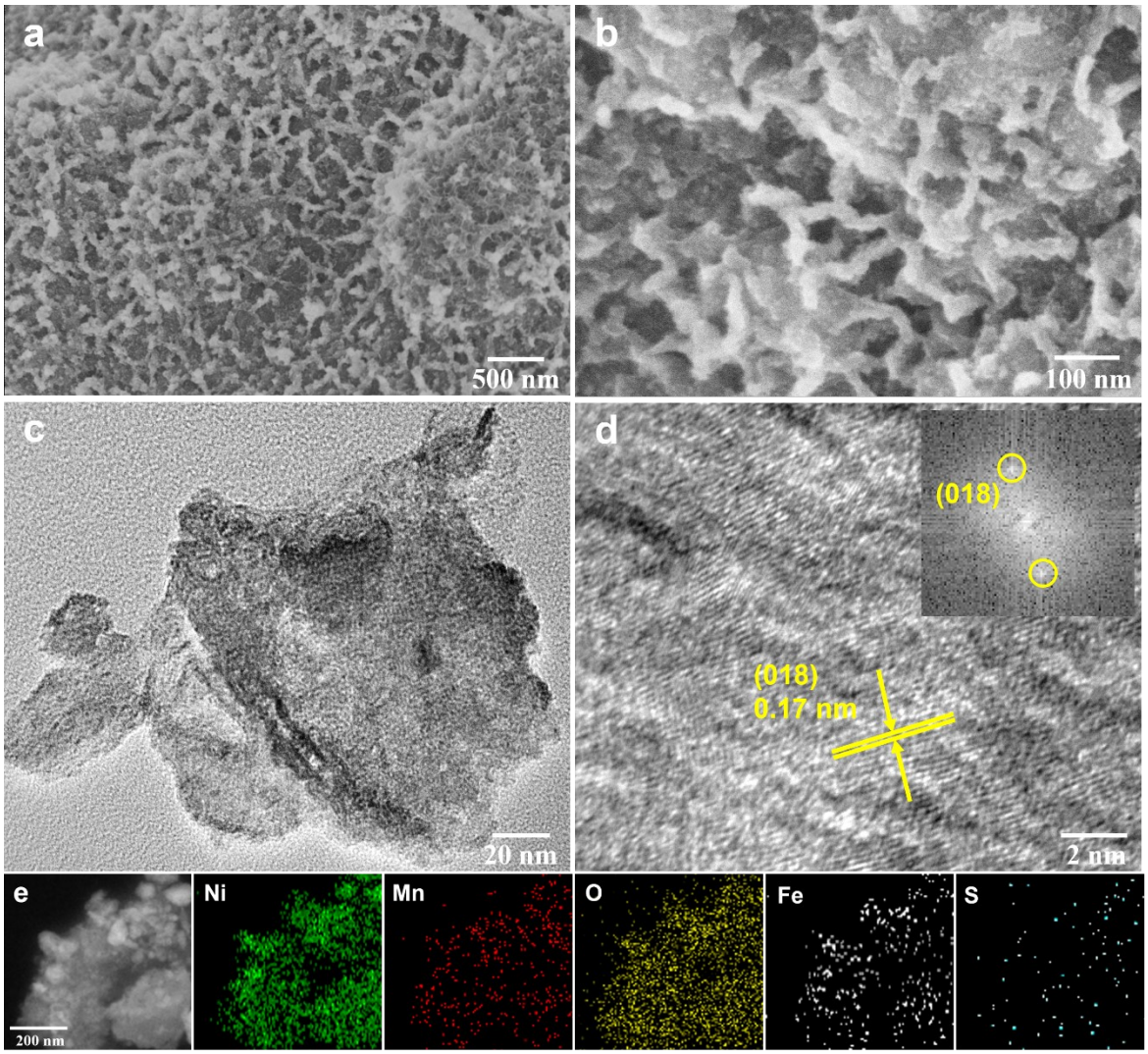

Figure S22. (a,b) SEM images, (c,d) TEM images, and (e) TEM-EDS elemental mapping of D-NiMn LDH/FeS after 20h OER test; Inset of d show FFT pattern of the corresponding part.

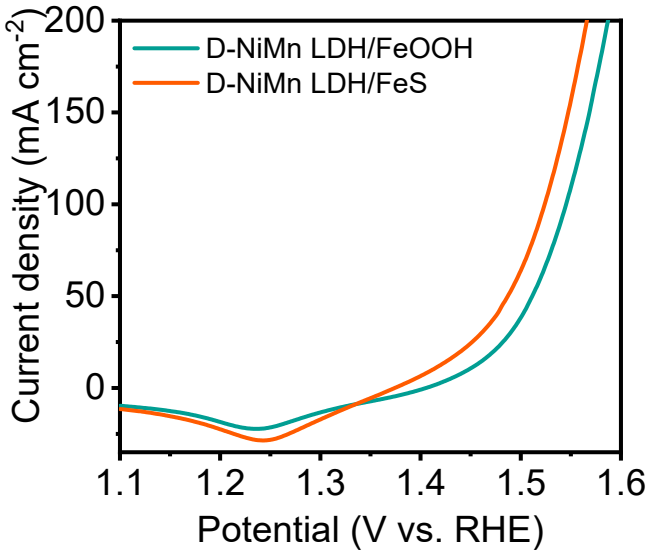

Figure S23. OER polarization curves of D-NiMn LDH/FeOOH and D-NiMn LDH/FeS.

To further explore the impact of S elements, we deposited FeOOH on D-NiMn LDH and conducted LSV tests. The results, shown in **Figure S23**, shows that the OER activity of D-NiMn LDH/FeOOH is improved (215 mV at 10 mA cm^{-2}), however, it is still lower compared to that of the D-NiMn LDH/FeS, indicating the crucial role of FeS in OER performance.

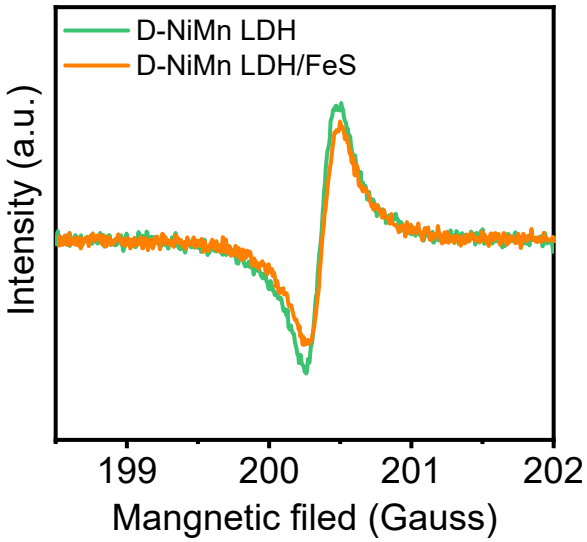

Figure S24. EPR spectra of D-NiMn LDH and D-NiMn LDH/FeS.

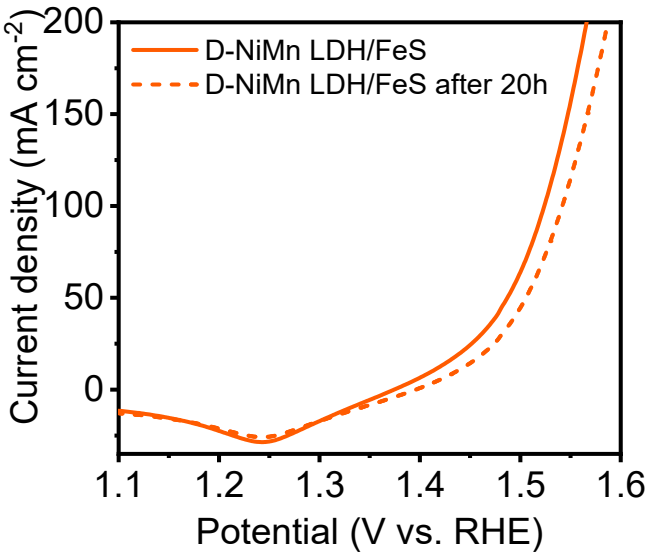

Figure S25. OER polarization curves of D-NiMn LDH/FeS before and after 20 h stability test.

We conducted further testing of the OER performance of D-NiMn LDH/FeS after the 20 h stability. As depicted in **Figure S25**, despite a declining trend in the activity of D-NiMn LDH/FeS after the stability test, it was still able to maintain an overpotential of 205 mV at 10 mA cm^{-2}.

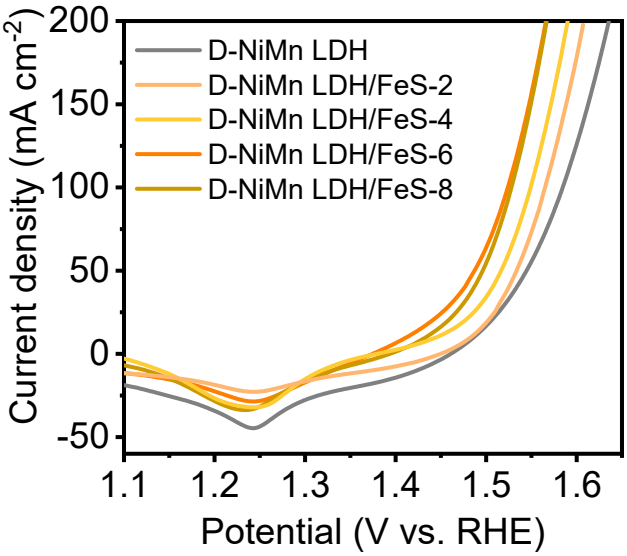

Figure S26. OER polarization curves of the catalysts.

In order to determine the optimal FeS ratio, we conducted successive ionic layer adsorption and reaction (SILAR) cycles of D-NiMn LDH, performing 2, 4, 6, and 8 cycles, respectively. This process resulted in D-NiMn LDH samples with varying FeS loading mass, denoted as D-NiMn LDH/FeS-2, D-NiMn LDH/FeS-4, D-NiMn LDH/FeS-6, and D-NiMn LDH/FeS-8. **Figure S26** demonstrates a gradual enhancement in the OER performance with an increase in the number of cycles, reaching its optimal performance at 6 cycles.